

# Estimating breast thickness for dual-energy subtraction in contrast-enhanced digital mammography using calibration phantoms

Kristen C. Lau<sup>1</sup>, Young Joon Kwon, Moez Karim Aziz, Raymond J. Acciavatti, Andrew D. A. Maidment  
University of Pennsylvania, Department of Radiology, 3400 Spruce Street, Philadelphia, PA 19104 USA

## ABSTRACT

Dual-energy contrast-enhanced digital mammography (DE CE-DM) uses an iodinated contrast agent to image the perfusion and vasculature of the breast. DE images are obtained by a weighted logarithmic subtraction of the high-energy (HE) and low-energy (LE) image pairs. We hypothesized that the optimal DE subtraction weighting factor is thickness-dependent, and developed a method for determining breast tissue composition and thickness in DE CE-DM. Phantoms were constructed using uniform blocks of 100% glandular-equivalent and 100% adipose-equivalent material. The thickness of the phantoms ranged from 3 to 8 cm, in 1 cm increments. For a given thickness, the glandular-adipose composition of the phantom was varied using different combinations of blocks. The logarithmic LE and logarithmic HE signal intensities were measured; they decrease linearly with increasing glandularity for a given thickness. The signals decrease with increasing phantom thickness and the x-ray signal decreases linearly with thickness for a given glandularity. As the thickness increases, the attenuation difference per additional glandular block decreases, indicating beam hardening. From the calibration mapping, we have demonstrated that we can predict percent glandular tissue and thickness when given two distinct signal intensities. Our results facilitate the subtraction of tissue at the boundaries of the breast, and aid in discriminating between contrast agent uptake in glandular tissue and subtraction artifacts.

**Keywords:** breast imaging, contrast-enhanced, dual-energy, glandularity, image subtraction, mammography

## 1. INTRODUCTION

The observation that angiogenesis accompanies the development of cancer provides the motivation for contrast-enhanced breast imaging. Contrast-enhanced digital mammography (CE-DM) uses an iodinated contrast agent to image the perfusion and vasculature of the breast. This imaging modality has emerged as an alternative to CE-MRI, the current gold standard, for imaging breast cancer perfusion and the characterization of lesions in the diagnosis of breast cancer. CE-MRI is used to screen women who have a high risk of developing breast cancer, as well as evaluating the extent of disease in diagnostic imaging. CE-DM has great potential to improve the detection and diagnosis of breast cancer by combining morphologic and functional information on vascular kinetics in a single examination. Unlike MRI, microcalcifications are better visualized in CE-DM. It is also possible to exploit the linear relationship between the attenuation coefficient and the concentration of contrast agent in CE-DM.

Contrast uptake by breast tissue is made more evident by dual-energy (DE) subtraction. Low-energy (LE) and high-energy (HE) image pairs are acquired in DE x-ray breast imaging. Two distinct x-ray energies are used to differentiate the linear attenuation coefficient of the contrast agent signal from the soft tissue signal. The x-ray energies are chosen so that the k-edge of the contrast agent lies within the range spanned by the LE and HE x-ray spectra. Patient motion is minimized in DE subtraction because the HE and LE image pairs are acquired almost simultaneously. A weighted difference of the logarithms of the LE and HE images is performed with the goal of cancelling background breast tissue to increase enhancement conspicuity. The DE signal intensity  $S^{DE}$  is expressed as

$$S^{DE} = \ln(S^{HE}) - w * \ln(S^{LE}) \quad (1)$$

where  $w$  is the DE weighting factor,  $S^{HE}$  is the signal intensity of the HE image, and  $S^{LE}$  is the signal intensity of the LE image. The weighting factor,  $w$ , is calculated to eliminate the dependence of the DE signal on the glandular-adipose signal of the breast tissue, and it is expressed as

$$w = \frac{\mu_a^{HE} - \mu_g^{HE}}{\mu_a^{LE} - \mu_g^{LE}} = \frac{\ln(S_a^{HE}) - \ln(S_g^{HE})}{\ln(S_a^{LE}) - \ln(S_g^{LE})} \quad (2)$$

<sup>1</sup> Kristen.Lau@uphs.upenn.edu, Raymond.Acciavatti@uphs.upenn.edu, Andrew.Maidment@uphs.upenn.edu

where  $\mu$  is the linear attenuation coefficient and the subscripts  $a$  and  $g$  represent adipose tissue and glandular tissue, respectively. This is based on the work of Karunamuni *et al.* [1].

Current methods for DE subtraction use a constant weighting factor. However, this does not consider the thickness of the compressed breast. We have developed a method for determining breast thickness and composition in DE CE-DM. The motivation for our work arises from the difficulty in resolving contrast uptake at the boundaries of the breast in DE subtraction. A number of studies have noted the presence of subtraction artifacts in DE CE-DM and their impact on image interpretation. Yagil *et al.* [2] classify these artifacts into four categories: rim, ripple, axillary line, and skin-line artifacts.

We hypothesize that the optimal weighting factor is thickness-dependent. Therefore, weighting factors near the periphery of the breast, where the breast is thinner, should be different from those in the center. Methods for quantification of breast composition using DE mammography have been explored by Ducote *et al.* [3] and Laidevant *et al.* [4]. However, these methods require the use of a calibration phantom and do not quantitatively determine the breast thickness. By quantifying the breast thickness and composition as a function of position, we can optimize our DE subtraction by finding the optimal weighting factor at each pixel location.

## 2. METHODS

We first simulated software tissue phantoms to investigate the relationship between DE subtraction and tissue thickness. We then performed a calibration experiment using physical phantoms constructed from breast tissue-equivalent materials. The calibration allowed us to develop a mathematical model to quantitatively determine breast thickness and composition from signal intensities. Finally, we used a physical anthropomorphic breast phantom to test our mathematical model.

### 2.1 Simulation

Polyenergetic x-ray spectra were generated using the TASMIP (tungsten anode spectral model using interpolating polynomials) simulation software developed by Boone *et al.* [5]. The software simulates x-ray spectra at 1 keV intervals over the range from 30 kV to 140 kV. X-ray energies were chosen so the k-edge of iodine (33.2 keV) was in the range spanned by the LE and HE x-ray spectra. To model the DE Hologic Selenia Dimensions DBT clinical protocol, the LE spectra was chosen to be 32 kV and the HE spectra was chosen to be 49 kV.

Breast tissue was modeled by simulating phantoms consisting of a uniform composition of glandular-equivalent and adipose-equivalent materials. The thickness of the phantoms ranged from 0.5 to 10 cm, in 0.5 cm increments. For a given thickness, the glandular-adipose composition of the phantom was varied in 10% increments from 0% glandularity to 100% glandularity (Figure 1).

Given the incident number of photons,  $N_0$ , from an x-ray beam, the number of photons transmitted through a phantom,  $N_{ph}$ , at a specific energy bin,  $E$ , is given by the Beer-Lambert law as

$$N_{ph}(E) = N_0(E) e^{-(\mu_g m_g + \mu_a m_a) \Delta t} \quad (3)$$

where  $\Delta t$  is the phantom thickness,  $\mu$  is the linear attenuation coefficient,  $m$  is the percent tissue composition, and the subscripts  $a$  and  $g$  represent adipose tissue and glandular tissue, respectively. The glandular and adipose tissue compositions are related by

$$m_g + m_a = 1. \quad (4)$$

We modeled an energy-integrating selenium detector in our simulation, and the signal intensity of the phantom,  $S_{ph}$ , is determined by

$$S_{ph} = \sum_{E}^{E_{\max}} N_{ph}(E) * E * e^{-\mu_{Se} t_{Se}} \quad (5)$$

where  $E_{\max}$  is equal to the simulated tube potential,  $\mu_{Se}$  is the linear attenuation coefficient of selenium, and  $t_{Se} = 0.5$  mm is the thickness of the selenium. The DE signal intensity for each phantom was determined using the DE subtraction method detailed in Section 1.

## 2.2 Calibration

To test our simulation experimentally, we performed a calibration using physical tissue-equivalent phantoms. Phantoms were constructed using 1 cm thick uniform blocks of 100% glandular-equivalent and 100% adipose-equivalent materials (CIRS, Norfolk, VA). The thickness of the phantoms ranged from 3 to 8 cm, in 1 cm increments. Each block measured 24 cm × 30 cm. For a given thickness, the glandular-adipose composition of the phantom was varied using different combinations of blocks (Figure 1). This differs from our simulation model in that only certain glandularities are achievable at a given calibration phantom thickness due to the discrete thickness of the individual uniform blocks.

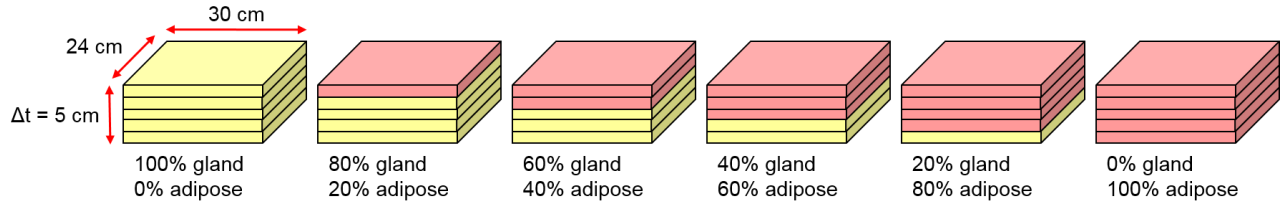


Figure 1. Example of a 5 cm phantom. The glandularity of the calibration phantom was varied in 1 cm increments by varying the combination of the blocks. The adipose tissue is depicted in yellow and the glandular tissue in red.

The phantoms were imaged using a prototype DE Hologic Selenia Dimensions DBT system. A 0.3 mm copper filter was used for the HE images (49 kV) and a 0.7 mm aluminum filter was used for the LE images (32 kV). X-ray energies were chosen so the k-edge of iodine (33.2 keV) was in the range spanned by the LE and HE x-ray spectra. The mAs (exposure) was varied to accommodate phantoms of different thickness and to ensure adequate signal to the detector. Each phantom was imaged twice and the images were averaged to account for the variations in x-ray tube output. DE images of the phantoms were obtained using the subtraction method detailed in Section 1.

Analysis of the HE and LE phantom images was performed using MATLAB (MathWorks, Natick, MA). The images were smoothed using a 2D convolution with a 4×4 matrix prior to quantitative analysis. The convolution procedure minimizes the influence of outlier pixels. The LE and HE images were normalized by the mAs to account for variations in the signal intensity at different thicknesses. The mean intensity and standard deviation values were measured for a region of interest (ROI) in the normalized, logarithmic LE and HE images. The size of the ROI was chosen to be the central 25% of the total image area.

Using the calibration data, we developed a mathematical model to transform data in the LE-HE space into the glandularity-thickness space. This model allows us to quantitatively determine thickness and breast composition from two distinct signal intensities. We first modeled a logarithmic signal intensity,  $S$ , as a function of glandularity,  $g$ , at a constant thickness,  $t$ . Taking into account the dependency on thickness, the slope of this function can be represented by the partial derivative

$$\frac{\partial S}{\partial g} = c_1 + c_2 t \quad (6)$$

where  $c_1$  and  $c_2$  are constants. Solving for  $S$ , we obtain the expression

$$S = (c_1 + c_2 t)g + F(t) \quad (7)$$

The signal intensity can also be represented as a function of thickness. Similarly, the slope of this function can be given by a partial derivative with  $c_3$  and  $c_4$  as constants

$$\frac{\partial S}{\partial t} = c_3 + c_4 g \quad (8)$$

Combining equations (7) and (8), we obtain the differential equation

$$\frac{dF}{dt} = c_3 + (c_4 - c_2)g \quad (9)$$

The differential equation reduces to

$$\frac{dF}{dt} = c_3 \quad (10)$$

since  $F(t)$  does not depend on  $g$ , and it has the solution

$$F(t) = c_3t + c_0. \quad (11)$$

Therefore the signal intensity  $S$  can be written as a function of thickness and glandularity by substituting the solution (11) into (7) to obtain

$$S = c_0 + c_1g + c_2gt + c_3t. \quad (12)$$

If we extend this result to DE imaging, we can express the logarithmic LE and HE signal intensities,  $S^{LE}$  and  $S^{HE}$  respectively, as functions of glandularity and thickness

$$S^{HE} = \alpha_0 + \alpha_1g + \alpha_2gt + \alpha_3t \quad (13)$$

$$S^{LE} = \beta_0 + \beta_1g + \beta_2gt + \beta_3t. \quad (14)$$

The  $\alpha$  and  $\beta$  constant terms are found by fitting the HE and LE calibration data to three-dimensional surfaces given by equations (13) and (14).

The solution for  $t$  is a quadratic equation of the form

$$At^2 + Bt + C = 0. \quad (15)$$

Thus, solving for  $t$ , we obtain

$$t = \frac{-B \pm \sqrt{B^2 - 4AC}}{2A}, \quad t > 0 \quad (16)$$

where A, B, and C are represented by

$$A = \alpha_2\beta_3 - \alpha_3\beta_2 \quad (17)$$

$$B = \beta_2S^{HE} - \alpha_2S^{LE} + \alpha_1\beta_3 + \alpha_2\beta_0 - \alpha_3\beta_1 - \alpha_0\beta_2 \quad (18)$$

$$C = \beta_1S^{HE} - \alpha_1S^{LE} + \alpha_1\beta_0 - \alpha_0\beta_1. \quad (19)$$

It follows that glandularity can be calculated as a function of thickness from the expression

$$g = \frac{S^{HE} - \alpha_0 - \alpha_3t}{\alpha_1 + \alpha_2t}. \quad (20)$$

### 2.3 Validation with Physical Anthropomorphic Breast Phantom

We used a physical anthropomorphic breast phantom to test our calibration and to validate our mathematical transformation model (Figure 2). The phantom was designed by the X-Ray Physics Lab at the University of Pennsylvania and is fabricated and licensed by CIRS. The phantom is constructed of breast tissue-equivalent materials; it consists of six slabs, each providing a realistic arrangement of anatomical breast structures (i.e. the skin, Cooper's ligaments, and adipose and glandular tissue compartments). The phantom simulates a 450 mL breast with a compressed thickness of 5 cm and 17% volumetric breast density (excluding the skin) [6].

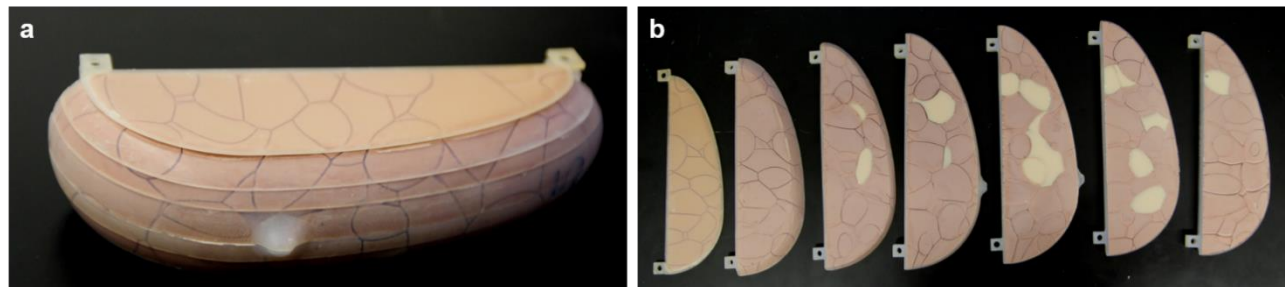


Figure 2. (a) Anthropomorphic breast phantom designed by the X-Ray Physics Lab. (b) Individual slabs of the breast phantom. Adipose (pink) and glandular (white) tissue compartments are visualized.

The physical breast phantom was imaged according to the clinical DE imaging protocol using a prototype DE Hologic Selenia Dimensions DBT system. A 0.3 mm copper filter was used for the HE image (49 kV, 72 mAs) and a 0.7 mm aluminum filter was used for the LE image (32 kV, 100 mAs).

The breast phantom images were processed in a manner similar to the tissue phantom images; images were smoothed using a 2D convolution with a 4×4 matrix prior to quantitative analysis. The LE and HE images were normalized by the mAs and the logarithms of the images were taken. Morphological filters (i.e. erosion) were used to eliminate the skin outline in the image. The thickness and composition of each pixel in the breast phantom were calculated using equations (14) and (18). The thickness and composition values for each pixel in the image were then spatially mapped to obtain thickness and composition images of the breast phantom.

### 3. RESULTS & DISCUSSION

#### 3.1 Tissue Phantom Simulation

The HE and LE spectra were generated using software simulation; the spectra were normalized by the mAs and are shown in Figure 4. The results from our tissue phantom simulation were plotted parametrically. The mean logarithmic HE intensity values were plotted against the mean logarithmic LE intensity values (Figure 3). The mean logarithmic LE and HE signal intensities vary with phantom thickness and glandularity. The mean logarithmic LE and HE signals decrease linearly with increasing glandularity for a given thickness. For each phantom thickness, a linear fit was modeled. The mean  $r^2$  for the linear fits is 0.999, indicating that a linear model is appropriate. It is important to note that the slope,  $\frac{\Delta S^{HE}}{\Delta S^{LE}}$ , of the linear fit is equal to the DE weighting factor,  $w$ . Thus, it is relevant to calculate the slope as a function of breast thickness.

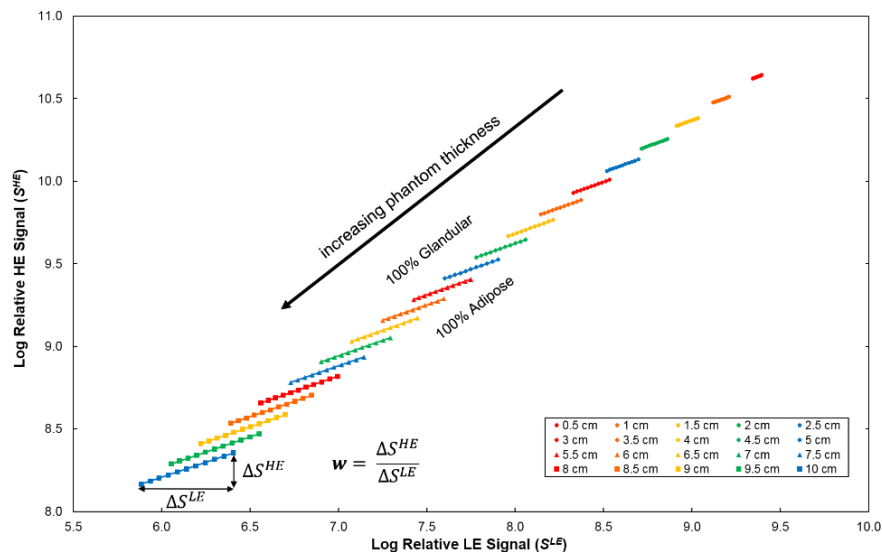


Figure 3. Signal intensities for software tissue phantoms of various thicknesses.

Upon closer inspection of the slopes of these linear fits, it is shown that the weighting factor,  $w$ , is thickness-dependent (Figure 5). For phantoms at least 2 cm thick, the  $w$  factor decreases linearly with increasing thickness. Given that we rarely encounter breasts with a compressed thickness less than 2 cm, a linear fit is likely sufficient.

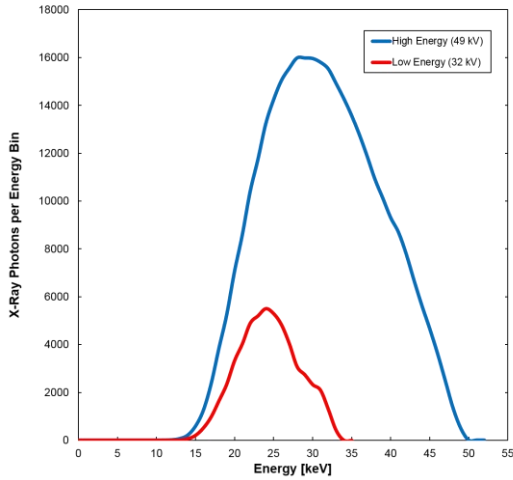


Figure 4. Generated x-ray spectra using software simulation. The HE spectrum is shown in blue and the LE spectrum is shown in red.

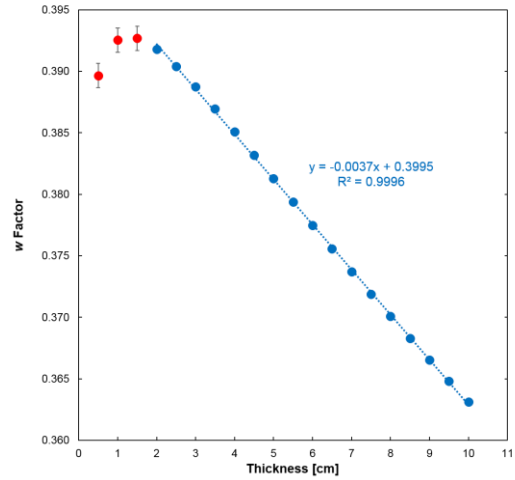


Figure 5. The DE weighting factor  $w$  is thickness-dependent. The red circles represent data for thicknesses less than 2 cm. These points were not included in the linear fit (blue line).

The LE and HE signals decrease with increasing phantom thickness and the x-ray signal decreases linearly with thickness for a given glandularity (Figure 6). For all thicknesses and for both energy levels, the signal intensity demonstrates a linear relationship with respect to percent glandularity. The mean  $r^2$  for the LE linear fits is 0.998 and the mean  $r^2$  for the HE linear fits is 0.989. For each energy, the linear fits extrapolate back to a common point at zero thickness, which is an expected result. The effective attenuation difference decreases as the phantom thickness increases, indicating beam hardening (Figure 7).

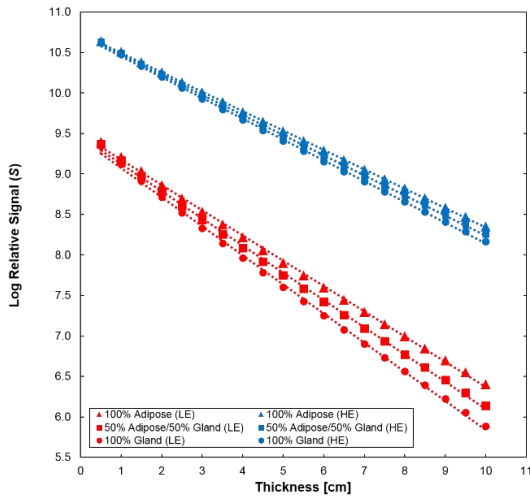


Figure 6. Signal intensities for phantoms of various glandularities at HE and LE.

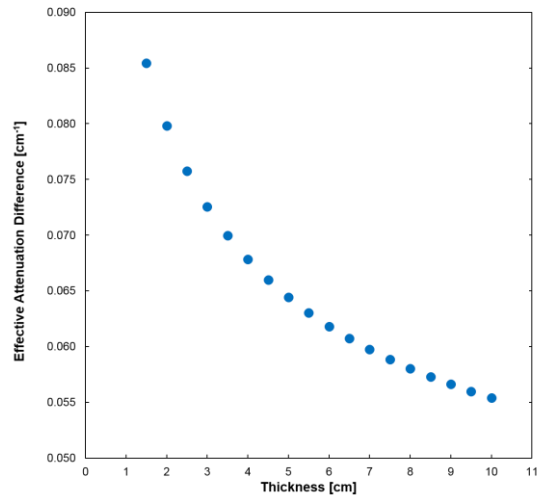


Figure 7. Impact of tissue composition on signal demonstrates beam hardening.

### 3.2 Calibration Tissue Phantom Experiment

Physical tissue-equivalent phantoms were imaged to validate our software simulation. For each energy and for each thickness, the signal intensity was plotted against percent glandularity. For all thicknesses and for both energy levels, the signal intensity demonstrates a linear relationship with respect to percent glandularity (Figure 8). The mean  $r^2$  for the LE linear fits is 0.998 and the mean  $r^2$  for the HE linear fits is 0.989. The results also demonstrate that for a given thickness, points along the linear fit line are equidistantly spaced apart.

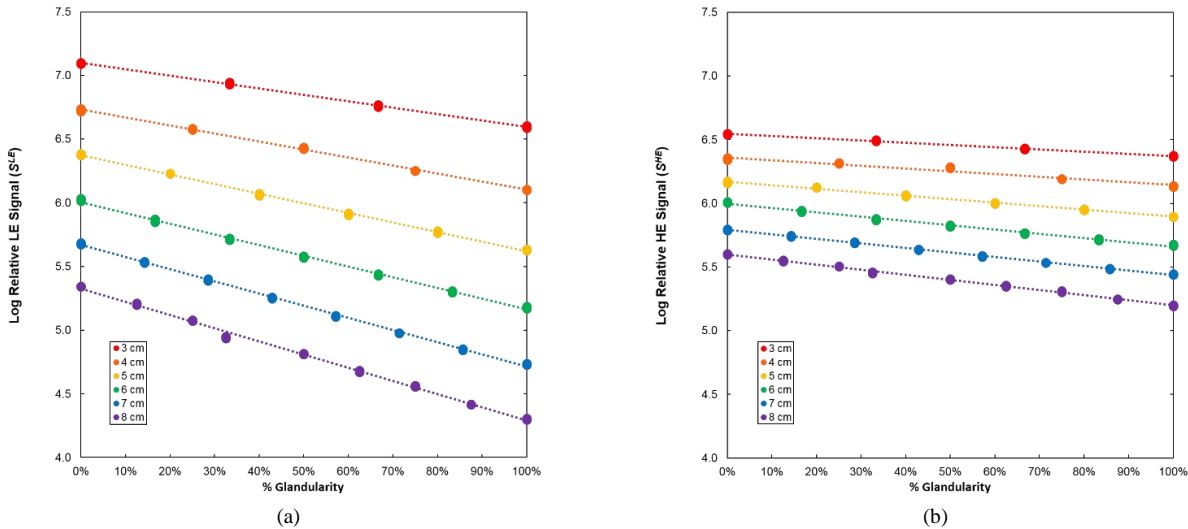


Figure 8. The linear relationship between the logarithm of the signal intensity and percent glandularity for phantoms of various thicknesses at (a) low-energy and (b) high-energy.

For each energy and for each glandularity, the signal intensity was plotted against thickness (Figure 9). Glandularities with a single data point are represented by a pink triangle. A linear fit was modeled for all glandularities that had at least two data points. For both energy levels, the signal intensity demonstrates a linear relationship with respect to thickness. A limitation of this analysis is the limited number of data points for certain glandularities due to the discrete thickness of the uniform blocks used to construct the tissue calibration phantoms. This limitation can be addressed by using thinner uniform blocks to construct the tissue calibration phantoms.

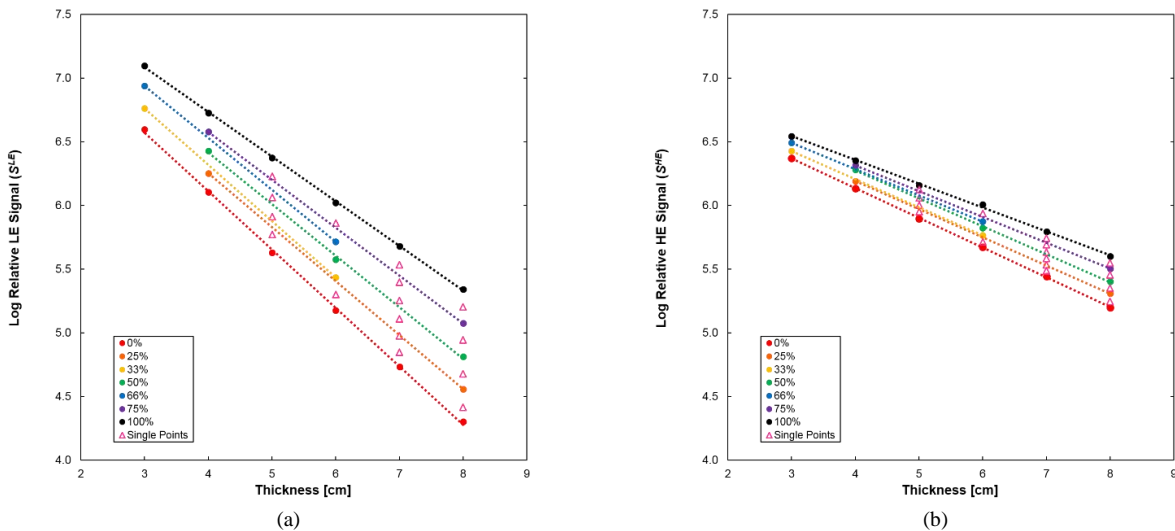


Figure 9. The linear relationship between the logarithm of the signal intensity and thickness for phantoms of various glandularities at (a) low-energy and (b) high-energy. The pink triangles represent glandularities with only a single data point.

If we consider the slope of the linear fits in the signal intensity versus percent glandularity plots (Figure 8) for each thickness, the slope of each fit is  $\partial S / \partial g$ . For both energies,  $\partial S / \partial g$  was plotted against thickness, demonstrating a linear relationship (Figure 10a). This linear relationship validates the assumption of equation (6) in which the slope of the signal intensity function is dependent on thickness.

Similarly, the slope of the linear fits in the signal intensity versus thickness plots (Figure 9) for each thickness is  $\partial S / \partial t$ .  $\partial S / \partial t$  was plotted against thickness for each glandularity at both energies and a linear relationship was demonstrated

(Figure 10b). This linear relationship validates the assumption of equation (8) in which the slope of the signal intensity function is dependent on glandularity.

Our mathematical model was developed based upon the assumptions of equations (6) and (8). These assumptions were validated experimentally as shown in Figure 10. Therefore, equations (6) and (8) became the starting point for the mathematical transformation model by using the solutions to the differential equations to solve for the HE and LE signal intensities ( $S^{HE}$  and  $S^{LE}$  respectively).

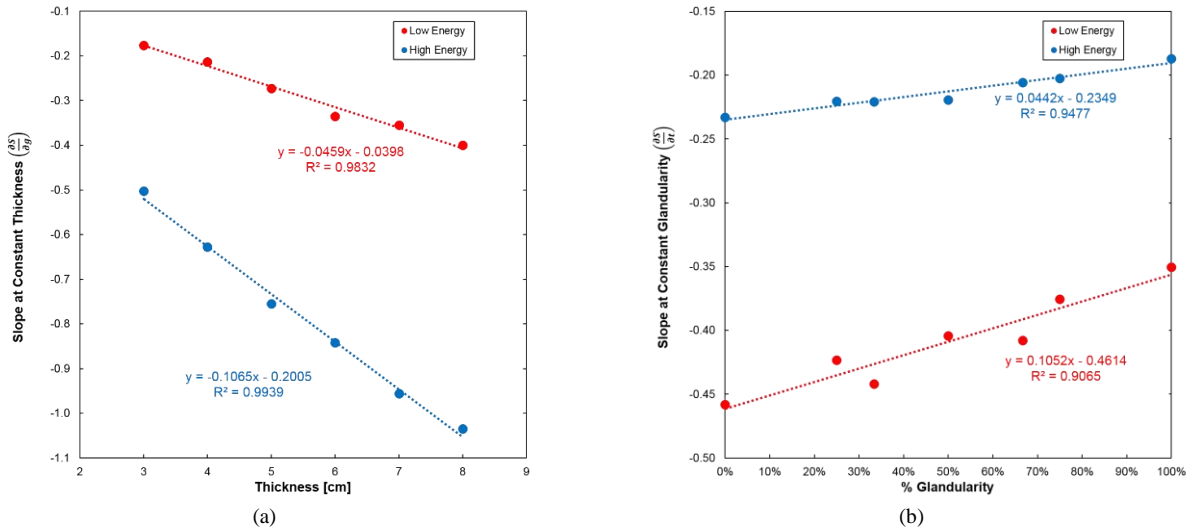


Figure 10. Validation of assumptions used to develop the mathematical transformation model. (a) Plot of  $\partial S/\partial g$  versus thickness for both HE and LE. (b) Plot of  $\partial S/\partial t$  versus percent glandularity for both HE and LE.

The results obtained from the physical tissue phantom experiments are concordant with those found by simulation. The mean logarithmic HE intensity values were plotted parametrically against the mean logarithmic LE intensity values (Figure 11). The mean logarithmic LE and HE signal intensities vary with phantom thickness and glandularity. The mean logarithmic LE and HE signals decrease linearly with increasing glandularity for a given thickness. For each phantom thickness, a linear fit was modeled. The mean  $r^2$  for the linear fits is 0.995, indicating a good linear model for the data. The  $r^2$  of the linear fits ranged from 0.974 to 0.999. Similarly, the slope of this linear fit represents the DE weighting factor,  $w$ , which is dependent on thickness (Figure 12).

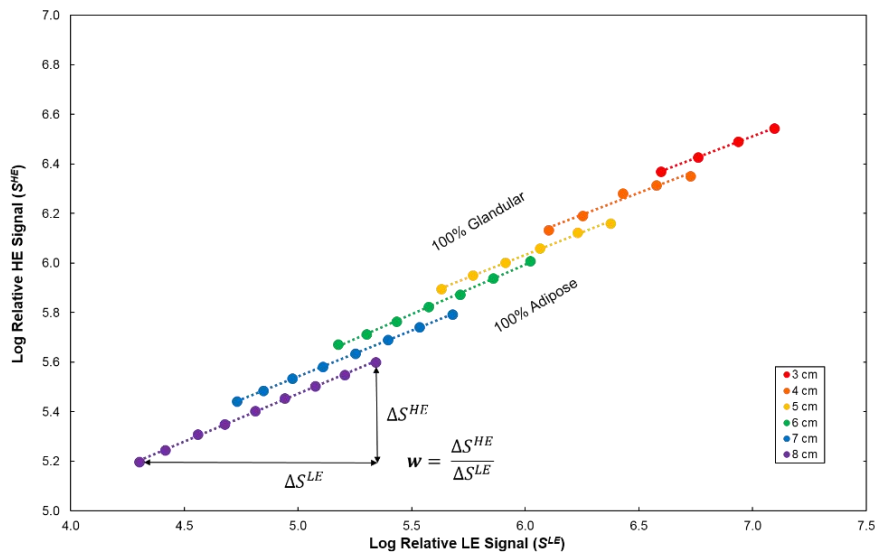


Figure 11. Signal intensities for calibration tissue phantoms of various thicknesses.

If we consider that DE subtraction has the purpose of projecting a LE-HE signal pair down to a single value, it can be shown in that every thickness has a distinct DE signal (Figure 13). This result is nontrivial. In Figure 13, each circle represents a LE-HE signal pair and each color represents a different thickness. Each thickness has a distinct DE signal because DE subtraction intrinsically encodes breast thickness information when using the common weighting scheme, which is designed to eliminate the signal between glandular and adipose tissues. Additionally, as shown earlier, the slopes of the thickness lines are distinct. This supports the use of a more detailed calibration approach.

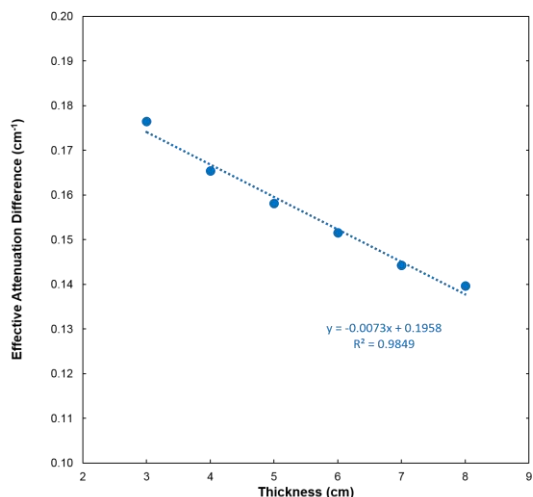


Figure 12. The DE weighting factor is thickness dependent.

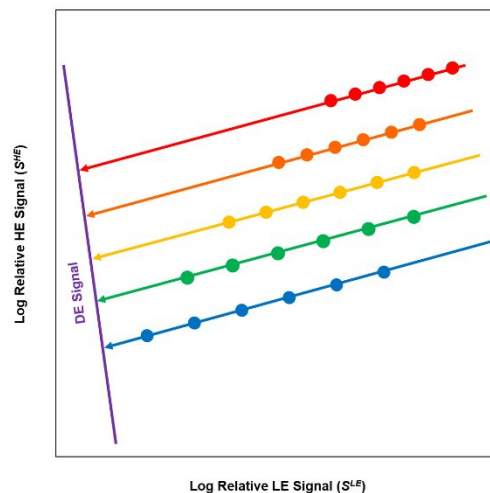


Figure 13. Illustration of signal intensity pairs projected onto DE signal space (purple line).

### 3.3 Validation of Transformation Model

#### 3.3.1 Tissue Phantom Simulation

We applied the model detailed in Section 2.2 to the simulation data and plotted these results (Figure 14). The blue diamonds represent the ground truth and the green circles represent the transformed measurements. A red line connects corresponding ground truth and calculated value pairs. The model was able to predict tissue thickness accurately, with a RMS error of 0.004 cm. Similarly, tissue glandularity was predicted accurately with a RMS error of 2.1%.

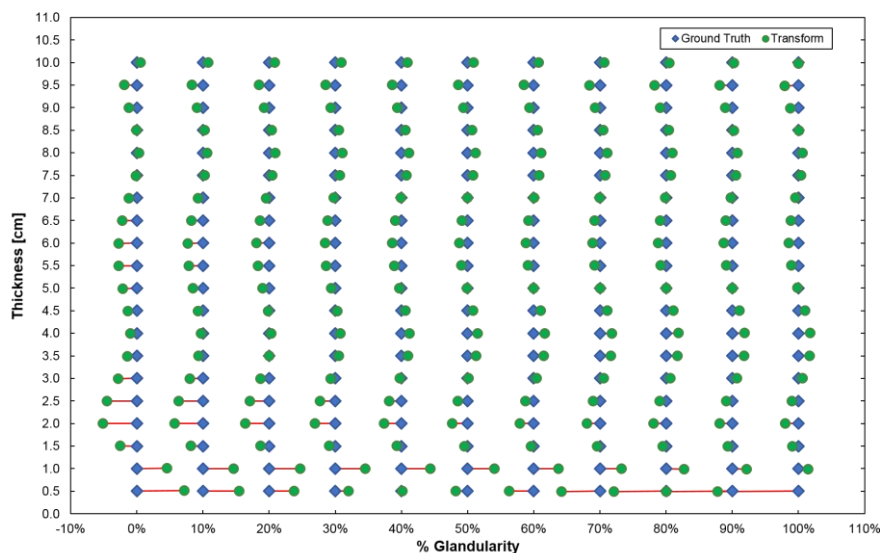


Figure 14. Result of transformation for simulation tissue phantom data from LE-HE space into thickness-glandularity space.

### 3.3.2 Calibration Tissue Phantom Experiment

The transformation model described in Section 2.2 was applied to the physical tissue phantom calibration data. These results are shown in Figure 15. The blue diamonds represent the ground truth and the green circles represent the transformed measurements. A red line connects corresponding ground truth and calculated value pairs. The model was able to predict tissue thickness accurately, with a RMS error of 0.13 cm. Tissue glandularity was predicted with a RMS error of 7.6%. These results support our claim that DE signal intrinsically encodes thickness information in an image. The discrepancies in glandularity prediction can be attributed to improper flat-fielding of the imaging system when acquiring the individual LE and HE images.

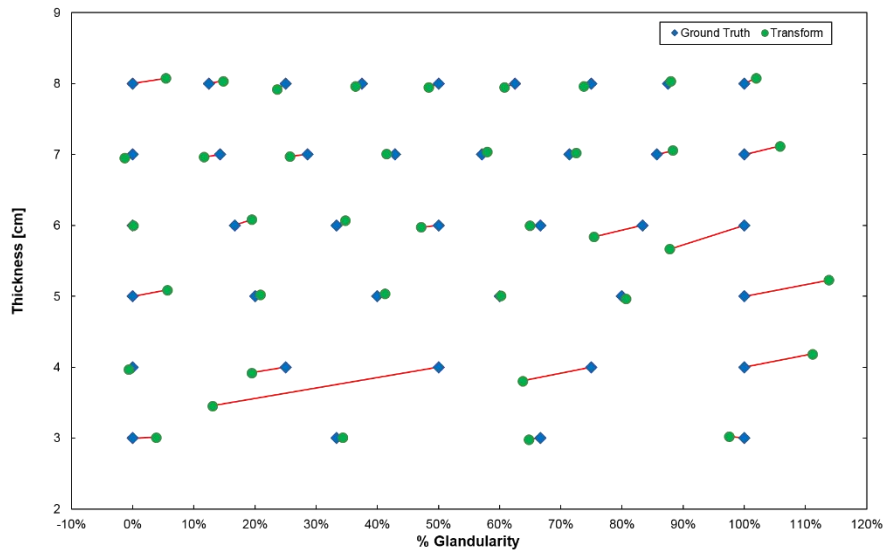


Figure 15. Result of transformation for experimental tissue phantom calibration data from LE-HE space into thickness-glandularity space.

### 3.4 Anthropomorphic Phantom

#### 3.4.1 Image Acquisition Parameters

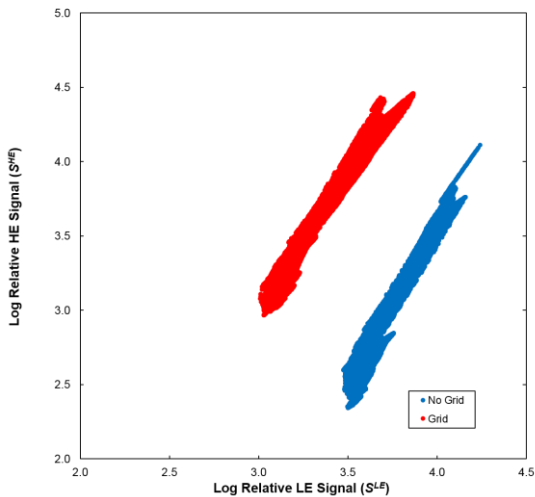


Figure 16. Result of imaging anthropomorphic breast phantom with and without a scatter grid. The point cloud representation of the phantom is shown.

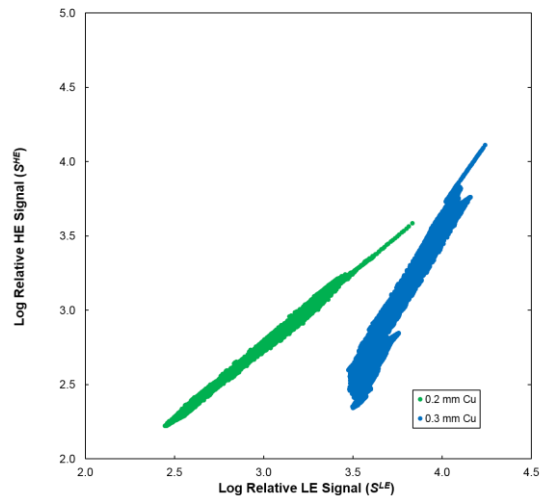


Figure 17. Result of imaging anthropomorphic breast phantom with different filters. The point cloud representation of the phantom is shown.

To test our mathematical transformation model, we imaged a physical anthropomorphic breast phantom. From our experiments, we arrived at two key results. Firstly, the calibration technique is dependent upon x-ray scatter. The breast phantom was imaged with and without a scatter grid. For every pixel in the phantom image, we plotted the logarithmic HE signal intensity versus the logarithmic LE signal intensity. We call this resulting plot a “point cloud”. The point cloud for the breast phantoms imaged with and without the scatter grid are shown in Figure 16. The grid is less effective with HE x-rays than with LE x-rays.

Secondly, the calibration technique is also dependent upon the filter used for the x-rays. As a demonstration, we imaged the phantom using a 0.2 mm copper filter and a 0.3 mm copper filter. The resulting point clouds for these images are shown in Figure 17.

### 3.4.2 Validation of Transformation Model Using a Physical Breast Phantom

We used the physical anthropomorphic breast phantom to validate our transformation model. The thickness and composition values for each pixel in the breast phantom were calculated and spatially mapped to obtain thickness and composition images. In the thickness image (Figure 18c), different regions of uniform thickness are represented by different colors. The thickest region in the interior of the breast is shown in white. As expected, the thickness changes sharply when projecting outwards toward the edges of the breast due to the breast curvature. Similarly, different regions of uniform glandularity are shown in different colors in the composition image (Figure 18d).

We recognize that improvements to the model are needed, as the transformation model is not yet complete. For example, the thickness image incorporates some glandularity information in the image. This could be attributed to possible differences in the composition of tissue-equivalent materials used in the physical breast phantom and calibration phantoms.

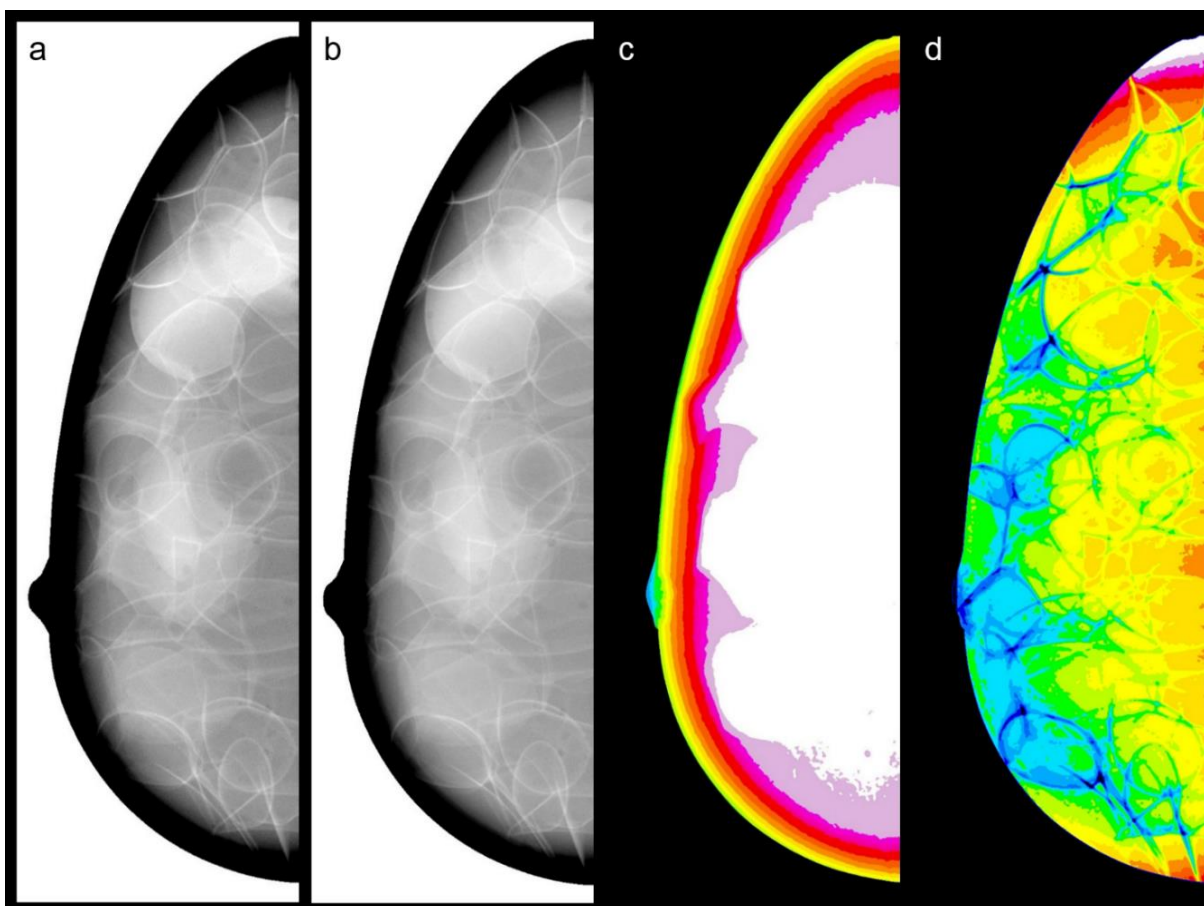


Figure 18. Physical anthropomorphic breast phantom images acquired using a DE CE-DM system at (a) HE = 49 kV and (b) LE = 32 kV. Results of transformation model for the breast phantom are shown in the (c) thickness and (d) composition images.

## 4. CONCLUSION

We have developed a method to determine breast tissue thickness and composition quantitatively in DE CE-DM. We have shown that breast thickness and composition can be predicted from the linear relationship between LE and HE signal intensities in DE CE-DM. We can do this because DE subtraction to null the glandular-adipose tissue signal intrinsically encodes thickness information. This has implications for the weighting factor used in DE subtraction for a given thickness. We have shown that the weighting factor,  $w$ , changes with thickness. Using the results from our study, we have developed a calibration curve and transformation model that allows us to predict percent glandular tissue and thickness when given two distinct signal intensities in DE imaging. These results facilitate the subtraction of tissue in the periphery of the breast, and aid in discriminating between contrast agent uptake in glandular tissue and subtraction artifacts. We have also shown that the transformation mapping is dependent upon the acquisition technique (i.e. kV, filter, use of scatter grid). Our theoretical model using simulation data was validated experimentally using physical phantoms.

As a further development of our study, we will extend our calibration model for DE subtraction in CE digital breast tomosynthesis. We will also explore the effects of beam hardening and scattering on thickness estimation. Validation of our calibration model with clinical breast images is forthcoming.

## ACKNOWLEDGEMENTS

The project described is supported in part by Grant Number UL1RR024134 from the National Center for Research Resources. Support for R.J.A. was provided by the Postdoctoral Fellowship Grant PDF14302589 from Susan G. Komen®. The content is solely the responsibility of the authors and does not necessarily represent the official views of the funding agencies. This work is also supported in part by the Institute for Translational Medicine and Therapeutics' (ITMAT) Transdisciplinary Program in Translational Medicine and Therapeutics. The prototype imaging system is provided to the University of Pennsylvania by Hologic (Bedford, MA) under a research agreement. The authors wish to acknowledge the assistance of Jing Zhenxue, Andy Smith, Barry Ren and Chris Ruth from Hologic for technical assistance.

## REFERENCES

- [1] R. Karunamuni and A. D. A. Maidment, "Search for novel contrast materials in dual-energy x-ray breast imaging using theoretical modeling of contrast-to-noise ratio," *Phys. Med. Biol.* **59**(15), 4311–4324 (2014) [doi:10.1088/0031-9155/59/15/4311].
- [2] Y. Yagil, A. Shalmon, A. Rundstein, Y. Servadio, O. Halshtok, and M. Gotlieb, "Challenges in contrast-enhanced spectral mammography interpretation: artefacts lexicon," *Clin. Radiol.* **71**(5), 450–457 (2016) [doi:10.1016/j.crad.2016.01.012].
- [3] J. L. Ducote and S. Molloy, "Quantification of breast density with dual energy mammography: An experimental feasibility study," *Med. Phys.* **37**(2), 793–801 (2010) [doi:10.1118/1.3284975].
- [4] A. D. Laidevant, S. Malkov, C. I. Flowers, K. Kerlikowske, and J. A. Shepherd, "Compositional breast imaging using a dual-energy mammography protocol," *Med. Phys.* **37**(1), 164 (2010) [doi:10.1118/1.3259715].
- [5] J. M. Boone and J. A. Seibert, "An accurate method for computer-generating tungsten anode x-ray spectra from 30 to 140 kV.," *Med. Phys.* **24**(11), 1661–1670 (1997) [doi:10.1118/1.597953].
- [6] L. Cockmartin, P. R. Bakic, H. Bosmans, A. D. A. Maidment, H. Gall, M. Zerhouni, and N. W. Marshall, "Power Spectrum Analysis of an Anthropomorphic Breast Phantom Compared to Patient Data in 2D Digital Mammography and Breast Tomosynthesis," *Breast Imaging: 12th Int. Work. IWDM 2014. Proceedings.* **8539**(1), 423–429 (2014) [doi:http://dx.doi.org/10.1007/978-3-319-07887-8\_59].